

# Journal of Geophysical Research: Space Physics

## RESEARCH ARTICLE

10.1002/2014JA020371

### Special Section:

New perspectives on Earth's radiation belt regions from the prime mission of the Van Allen Probes

### Key Points:

- SAPS simulation using BATS-R-US coupled with ring current model RAM-SCB
- Comparisons done with AMPERE, DMSP, and Van Allen Probes observations
- Captured the basic physics and mechanism of SAPS

### Correspondence to:

Y. Yu,  
yiqun@lanl.gov

### Citation:

Yu, Y., V. Jordanova, S. Zou, R. Heelis, M. Ruohoniemi, and J. Wygant (2015), Modeling subauroral polarization streams during the 17 March 2013 storm, *J. Geophys. Res. Space Physics*, 120, 1738–1750, doi:10.1002/2014JA020371.

Received 7 JUL 2014

Accepted 5 FEB 2015

Accepted article online 9 FEB 2015

Published online 12 MAR 2015

## Modeling subauroral polarization streams during the 17 March 2013 storm

Yiqun Yu<sup>1</sup>, Vania Jordanova<sup>2</sup>, Shasha Zou<sup>3</sup>, Roderick Heelis<sup>4</sup>, Mike Ruohoniemi<sup>5</sup>, and John Wygant<sup>6</sup>

<sup>1</sup>Applied Mathematics and Plasma Physics, Los Alamos National Laboratory, Los Alamos, New Mexico, USA, <sup>2</sup>Space Science and Application, Los Alamos National Laboratory, Los Alamos, New Mexico, USA, <sup>3</sup>Department of Atmospheric, Oceanic, and Space Sciences, University of Michigan, Ann Arbor, Michigan, USA, <sup>4</sup>Physics Department, University of Texas at Dallas, Dallas, Texas, USA, <sup>5</sup>Department of Electrical and Computer Engineering, Virginia Polytechnic Institute and State University, Blacksburg, Virginia, USA, <sup>6</sup>School of Physics and Astronomy, University of Minnesota, Minneapolis, Minnesota, USA

**Abstract** The subauroral polarization streams (SAPS) are one of the most important features in representing magnetosphere-ionosphere coupling processes. In this study, we use a state-of-the-art modeling framework that couples an inner magnetospheric ring current model RAM-SCB with a global MHD model Block-Adaptive Tree Solar-wind Roe Upwind Scheme (BATS-R-US) and an ionospheric potential solver to study the SAPS that occurred during the 17 March 2013 storm event as well as to assess the modeling capability. Both ionospheric and magnetospheric signatures associated with SAPS are analyzed to understand the spatial and temporal evolution of the electrodynamics in the midlatitude regions. Results show that the model captures the SAPS at subauroral latitudes, where Region 2 field-aligned currents (FACs) flow down to the ionosphere and the conductance is lower than in the higher-latitude auroral zone. Comparisons to observations such as FACs observed by Active Magnetosphere and Planetary Electrodynamics Response Experiment (AMPERE), cross-track ion drift from Defense Meteorological Satellite Program (DMSP), and in situ electric field observations from the Van Allen Probes indicate that the model generally reproduces the global dynamics of the Region 2 FACs, the position of SAPS along the DMSP, and the location of the SAPS electric field around L of 3.0 in the inner magnetosphere near the equator. The model also demonstrates double westward flow channels in the dusk sector (the higher-latitude auroral convection and the subauroral SAPS) and captures the mechanism of the SAPS. However, the comparison with ion drifts along DMSP trajectories shows an underestimate of the magnitude of the SAPS and the sensitivity to the specific location and time. The comparison of the SAPS electric field with that measured from the Van Allen Probes shows that the simulated SAPS electric field penetrates deeper than in reality, implying that the shielding from the Region 2 FACs in the model is not well represented. Possible solutions in future studies to improve the modeling capability include implementing a self-consistent ionospheric conductivity module from inner magnetosphere particle precipitation, coupling with the thermosphere-ionosphere chemical processes, and connecting the ionosphere with the inner magnetosphere by the stronger Region 2 FACs calculated in the inner magnetosphere model.

### 1. Introduction

Subauroral polarization streams (SAPS) [Foster and Burke, 2002] represent the westward convection equatorward of the typical auroral convection flows in the ionosphere and are one of the most important inner magnetosphere-ionosphere coupling processes. Observations have shown that they are highly structured equatorward of the auroral oval predominantly in the dusk-to-midnight sector. They can change ionospheric composition, contribute to the formation of storm-enhanced density, plasmaspheric plumes, and ionospheric midlatitude density troughs [e.g., Spiro et al., 1978; Anderson et al., 1991; Karlsson et al., 1998; Foster and Vo, 2002; Foster and Rideout, 2007; Zou et al., 2013; Foster et al., 2014]. The ionospheric location of SAPS is found to be correlated with the peak location of the ring current energy density and coincides with the earthward edge of the ion plasma sheet in the magnetosphere [Yeh et al., 1991; Foster and Vo, 2002; Southwood and Wolf, 1978]. When Region 2 field-aligned currents (FACs), caused by the misalignment of gradients in the ring current pressure and magnetic flux volume, flow into the ionosphere on the evening side, part of the Region 2 FACs flows into regions of low ionospheric conductivity, leading to large electric field in order to maintain current continuity. The electric field is associated with zonal plasma drift, i.e., SAPS [Foster and Burke, 2002]. The inner magnetospheric dynamics is therefore highly linked to the

configuration of SAPS in the subauroral ionosphere, which can further influence the electric potential in the ionosphere and magnetosphere and eventually the ring current particle convection. Studying how the SAPS emerge and evolve during disturbed time can aid our understanding of transport process in the ring current and plasma sheet particles as well as their coupling with the ionosphere.

Although observations of SAPS have been extensively carried out [e.g., Yeh *et al.*, 1991; Anderson *et al.*, 2001; Foster and Vo, 2002; Oksavik *et al.*, 2006; Wang *et al.*, 2008; Clausen *et al.*, 2012], few modeling efforts have been made to reproduce and understand the dynamical SAPS features [e.g., Garner *et al.*, 2004; Wang *et al.*, 2009; Ebihara *et al.*, 2009; Zheng *et al.*, 2008]. While empirical models of inner magnetospheric electric fields and magnetic fields [e.g., Goldstein *et al.*, 2005] can provide a statistical, averaged representation of the enhanced flow channels in the inner magnetosphere, first-principle inner magnetosphere models use plasma physics-based calculations and allow for comprehensive investigation of the coupled magnetosphere-ionosphere system from a global sense. Such a type of models includes Rice Convection Model-Equilibrium (RCM-E) [Lemon *et al.*, 2003], CRCM [Fok *et al.*, 2001], RAM-SCB [Jordanova *et al.*, 2006, 2010; Zaharia *et al.*, 2006], and RCM [Toffoletto *et al.*, 2003] coupled with a modified Dungey force-balanced magnetic field solver [Gkioulidou *et al.*, 2011]. These models calculate ring current particle distributions self-consistently with either electric field or magnetic field or both fields. In order to be capable of modeling midlatitude ionospheric electrodynamics such as SAPS, a comprehensive self-consistent coupling between physical processes such as the inner magnetospheric ring current dynamics, large-scale convection, and the global Region 2 FACs, is necessary. In some of these models, the magnetic field self-consistency is achieved by applying an equilibrium solver between magnetic fields and ring current pressure (e.g., RCM-E, RAM-SCB, and RCM with a Dungey solver); the electric field self-consistency is obtained from incorporating an ionospheric potential solver equatorward of the high-latitude model boundary (e.g., CRCM, RCM-E, and RCM with a Dungey solver) with the electric potential being calculated based on FACs mapped from the inner magnetosphere region. In this paper, we present a new self-consistent modeling effort to study inner magnetosphere dynamics, in which an inner magnetosphere model is two-way coupled to an MHD code together with an ionospheric electric potential solver that captures both Region 1 and Region 2 FACs. Section 2 describes the details of these models and the coupling infrastructure between them.

During the 17 March 2013 storm event, the SuperDARN (Super Dual Auroral Radar Network) arrays of HF radars observed the expansion of high-latitude convection to unusually low latitudes. Figure 1 shows the results of fitting the SuperDARN line-of-sight velocity data collected for the scan centered on 9:45 UT to an expansion of the electrostatic potential in terms of spherical harmonics as described by Ruohoniemi and Baker [1998]; vectors are shown where radars made direct measurements and, for clarity, the potential pattern is not drawn. On the morning side strong flows are seen to extend to the northern U.S. states. In the afternoon sector radar coverage is more limited; however, the available data are consistent with strong sunward plasma flow near a latitude of 54°. The DMSP (Defense Meteorological Satellite Program) F18 satellite measurements of particle precipitation and ion drift at  $\sim 800$  km indicate that the satellite encountered a SAPS region near this latitude around 10:12 UT, as indicated by the large, narrow velocity stream (black spike, within the orange circle) equatorward of the auroral precipitation boundary that is identified by the sharp increase in particle precipitation (blue to red) along the rising satellite trajectory.

This study is motivated by understanding the temporal and spatial evolution of the SAPS during the above magnetic storm, and by the goal of assessing and improving the capability of a state-of-the-art modeling framework in reproducing the subauroral electrodynamics and the inner magnetospheric dynamics associated with the SAPS. We simulate the 17 March 2013 storm event using upstream solar wind driving conditions, obtained from the ACE spacecraft and propagated to the boundary of the MHD code (i.e.,  $32 R_E$  upstream away from the Earth). Figure 2 shows the OMNI data for solar wind and interplanetary magnetic field (IMF) conditions and the SYM-H index during the storm period. Approximately at 6:00 UT, a coronal mass ejection (CME) driven shock arrived at the magnetosphere, characterized by a sudden enhancement in the solar wind dynamic pressure and a southward turning of IMF  $B_z$ . The SYM-H index reached the first minimum of  $-100$  nT at 10:00 UT and the second one of  $-130$  nT at 20:00 UT.

## 2. Model Description

The magnetosphere-ionosphere coupling physics is simulated by coupling several first-principle physics-based models, including a global MHD code Block-Adaptive Tree Solar-wind Roe Upwind Scheme

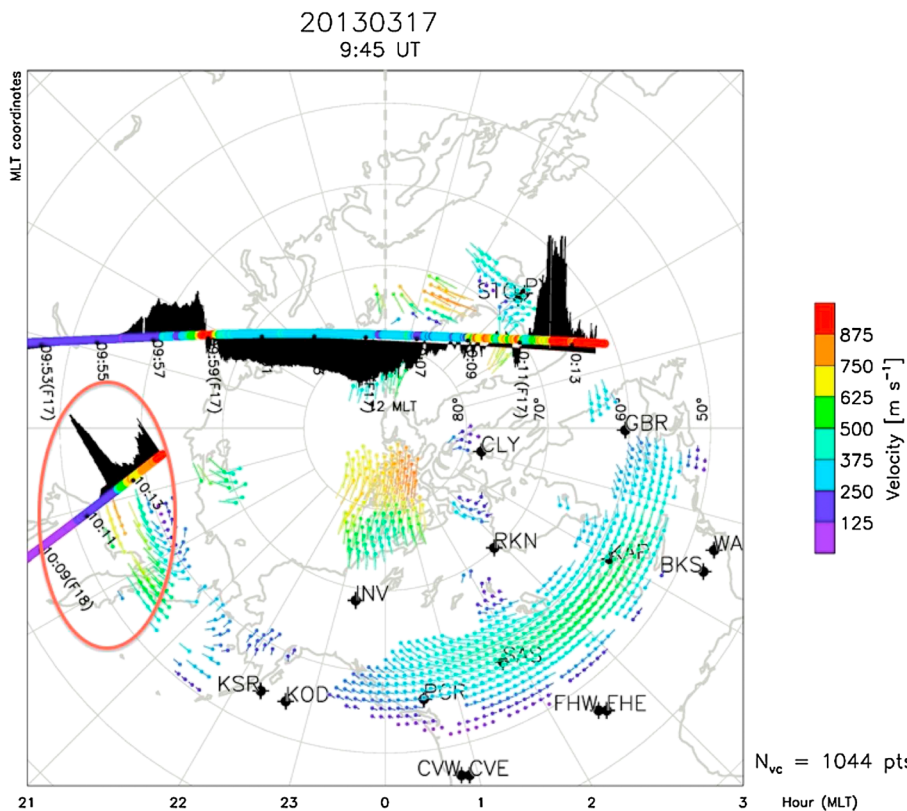


**Figure 1.** The SuperDARN radar observations on the Northern Hemisphere (color vectors) with two DMSP trajectories overplotted (F17 on the dayside and F18 near the dusk side). The color along the trajectories represents the intensity of electron precipitation flux. The black lines on the sides of the trajectories indicate the ion drift speed perpendicular to the orbit. The orange circle highlights the region where the SAPS are observed.

(BATS-R-US) [Powell *et al.*, 1999], a kinetic ring current model RAM-SCB [Jordanova *et al.*, 2006, 2010; Zaharia *et al.*, 2006], and an ionospheric electrodynamics solver [Ridley *et al.*, 2004]. The schematic illustration of the coupling infrastructure between these models is shown in Figure 3.

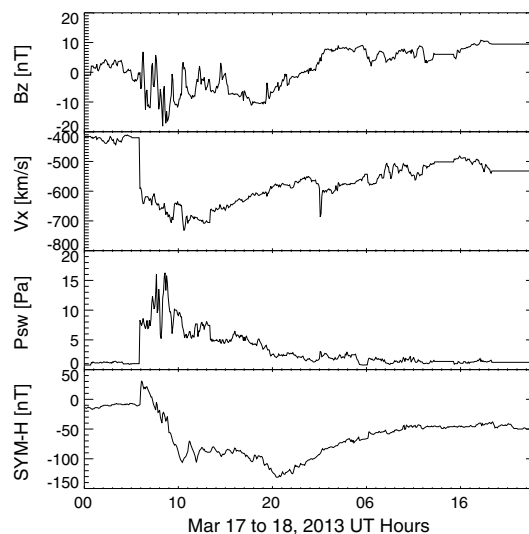


**Figure 2.** The OMNI data of the interplanetary magnetic field Z component, solar wind velocity, solar wind dynamic pressure, and SYM-H index during the magnetic storm on 17–18 March 2013.

The BATS-R-US code solves ideal MHD equations for the global magnetosphere and is coupled with the ionospheric electrodynamic solver at the ionospheric altitude of 100 km with cadence of 10 s: the FACs computed at  $3.5 R_E$  of the MHD code are mapped down to the ionospheric height, where the ionospheric electric potential is computed based on the FACs and ionosphere conductance. The electric potential is then mapped out to the inner boundary of the MHD code (i.e.,  $2.5 R_E$ ) to obtain the  $E \times B$  convection velocity as the inner boundary condition of the perpendicular velocity of the plasma in the MHD code.

The ionospheric electric potential solver has a low latitude boundary at  $\sim 20^\circ$  magnetic latitude. The ionospheric conductance used in the potential solver includes solar generated conductance,

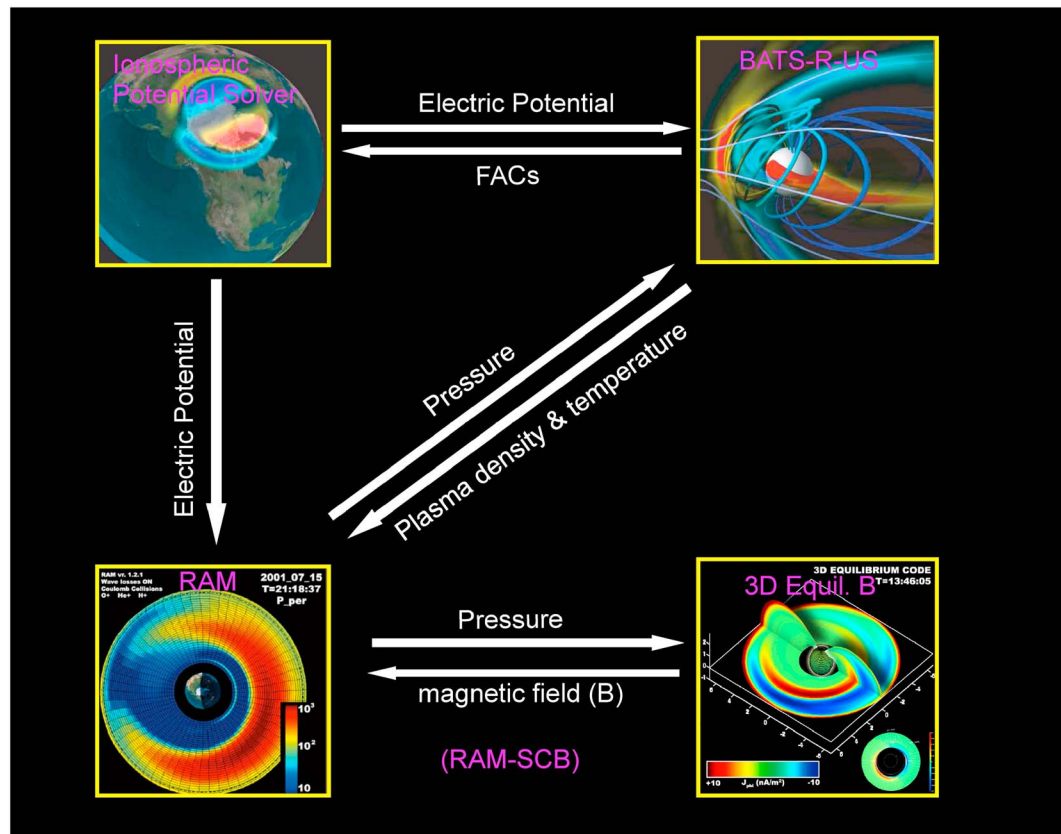


**Figure 3.** The schematic illustration of coupling infrastructure between the global MHD model BATS-R-US, the ionospheric electrodynamic solver, and the inner magnetosphere model RAM-SCB.

nightside conductance, and auroral zone conductance that is associated with particle precipitation. The solar illumination induces conductance on the dayside which depends on the F10.7 index and solar zenith angle. Nightside conductance is produced from ionization caused by star light and galactic sources. This ionization is added as a background uniform conductance over the entire globe. The auroral zone conductance is induced mostly from precipitating electrons and ions. All models need to specify the particle energy flux and characteristic energy in order to get conductance. In this model, the auroral conductance is specified through an empirical relationship with field-aligned currents. This relation was derived from the Assimilative Mapping of Ionospheric Electrodynamics (AMIE) technique [Richmond and Kamide, 1988], which generated thousands of maps of ionospheric Hall and Pedersen conductance and field-aligned currents based on solar conditions in 1997. From these maps, a relation between the local Hall/Pedersen conductance and field-aligned current was derived [Ridley et al., 2004]. Therefore, the auroral conductance in the ionosphere is highly dynamic during the course of a storm when field-aligned currents vary. Although this conductance is not directly derived from a first-principle description of particle precipitation, its relationship with the field-aligned current shows one approach of specifying the auroral conductance in MHD codes at present.

The MHD code and the ionospheric potential solver are also coupled with the RAM-SCB code that models the kinetic physics of charged particles in the inner magnetosphere inside  $6.5 R_E$ . The RAM-SCB couples the kinetic Ring current-Atmosphere Interactions model (RAM) with a 3-D Euler-potential-based plasma equilibrium code. The RAM code computes the bounce-averaged phase space distribution for  $H^+$ ,  $He^+$ ,  $O^+$ , and electrons in the magnetic equatorial plane as a function of radial distance ( $2 R_E$  to  $6.5 R_E$ ), all magnetic local times, energy ( $\sim 150$  eV to  $\sim 400$  keV), and pitch angle ( $0^\circ$  to  $90^\circ$ ). The loss processes for the ring current ions include charge-exchange with geocoronal hydrogen and collisions with the dense atmosphere, while losses due to atmosphere collisions and wave-particle interactions are considered for the electrons (see details in Jordanova et al. [2012]). The plasma pressure produced by the RAM ring current distribution

is used in the 3-D equilibrium code to calculate the force-balanced magnetic field, which is further used to propagate the phase space distribution function in RAM.

The ring current pressure is passed to the BATS-R-US code to modify the MHD pressure in the inner magnetosphere region, which subsequently changes the global magnetospheric configuration and current systems. In turn, the MHD code provides the plasma sheet source boundary condition (density and characteristic temperature) to the kinetic model at  $6.5 R_E$ . These boundary conditions are updated every 5 min. Since a single-fluid MHD code is used in this study while the inner magnetosphere model solves for multiple ion species (i.e.,  $H^+$ ,  $O^+$ , and  $He^+$ ), an empirical relationship obtained from Young *et al.* [1982] is used to ascribe the ion composition ratios at the boundary of  $6.5 R_E$ . An isotropic Kappa distribution is assumed with the characteristic temperature and densities for each ion species. The electron density is obtained by charge neutrality and the electron temperature is one seventh of the ion temperature in accordance with plasma sheet observations [Baumjohann *et al.*, 1989]. The magnetic field boundary condition needed for the 3-D equilibrium is determined from an empirical model T89 [Tsyganenko, 1989]. The electric field needed in RAM is obtained from the ionospheric potential solver by mapping the electric potential onto the inner magnetosphere magnetic equator every 10 s. The ring current model is thereafter driven by a self-consistent electric field in addition to its existent self-consistent magnetic field.

### 3. Simulation Results

#### 3.1. Ionospheric Electrodynamics

Figure 4 displays the simulated field-aligned currents, Pedersen conductance, electric potential, electric field, and plasma convection in the Northern Hemisphere at selected times such as the quiet time at 6:00 UT, time during the storm sudden commencement (SSC) at 07:00 UT, and two time cadences during the storm main phase (09:35 and 11:45 UT). In Figure 4a, at the quiet time (i.e., 06:00 UT) before the SSC, the classic FAC pattern is reproduced: the higher-latitude Region 1 FACs (downward in the dawn sector and upward in the dusk sector) and lower latitude Region 2 FACs (upward in the dawn sector and downward in the dusk sector), with the Region 2 FACs in much weaker magnitude. This is because the ring current in the magnetosphere is very weak and the pressure gradient, highly associated with the Region 2, is not large. During the disturbed time after the SSC (e.g., at and after 07:00 UT), both Region 1 and Region 2 FACs are clearly intensified and expand equatorward. In addition, the circular pattern of Region 2 FACs rotates westward as the storm develops, as much as 3 h in magnetic local time (see 11:45 UT). Subsequently, the orientation of the FACs, originally quasi-symmetric about the noon-midnight meridian, now rotates to around 21 magnetic local time (MLT). Such a rotation can be explained by the development of partial ring current in the inner magnetosphere which is described in the next section.

As the storm develops and field-aligned currents intensify, the auroral conductance (Figure 4b) is enhanced while the auroral zone expands equatorward. The electric potential in (Figure 4c) illustrate the typical two-cell pattern. During storm time, the evening potential cell expands to lower latitudes, indicating the penetration of the convection electric field to the subauroral region. It is found that the subauroral potential cell during largely disturbed time in the dusk-to-midnight sector demonstrates a tendency of separation from the higher-latitude auroral convection cell. The subauroral potential extends toward the postmidnight with the flow reversal in the Harang reversal region occurring around latitudes between 60 and 50°.

The tight potential contour lines around 60° near the dusk suggest large electric fields mainly in the poleward direction, as shown in Figure 4d. This poleward electric field displays two branches at postdusk local times, one at subauroral latitude separated from the one at higher auroral latitudes. The large electric field at the subauroral region is needed in order to maintain the current continuity because the conductivity in this subauroral latitude is lower compared to that in the auroral zone above 60°, while Region 2 FACs into this region increases during the storm. It is this large subauroral poleward electric field that corresponds to the rapid sunward plasma convection in the subauroral ionosphere near the dusk, as shown in Figure 4e. This sunward drift in the dusk sector is clearly seen at and after 07:00 UT, with the peak of the flow exceeding 1500 m/s. The flow channel extends into late local times with decreasing speed. These features are consistent with the averaged characteristics of SAPS [e.g., Anderson *et al.*, 2001; Foster and Burke, 2002; Foster and Vo, 2002; Clausen *et al.*, 2012]. The subauroral westward flow is nearly collocated with the lower latitude downward Region 2 FACs and the peak of the flow appears near the equatorward edge of the upward Region 1 FACs or electron precipitation, suggesting that the model captures the mechanism of SAPS.

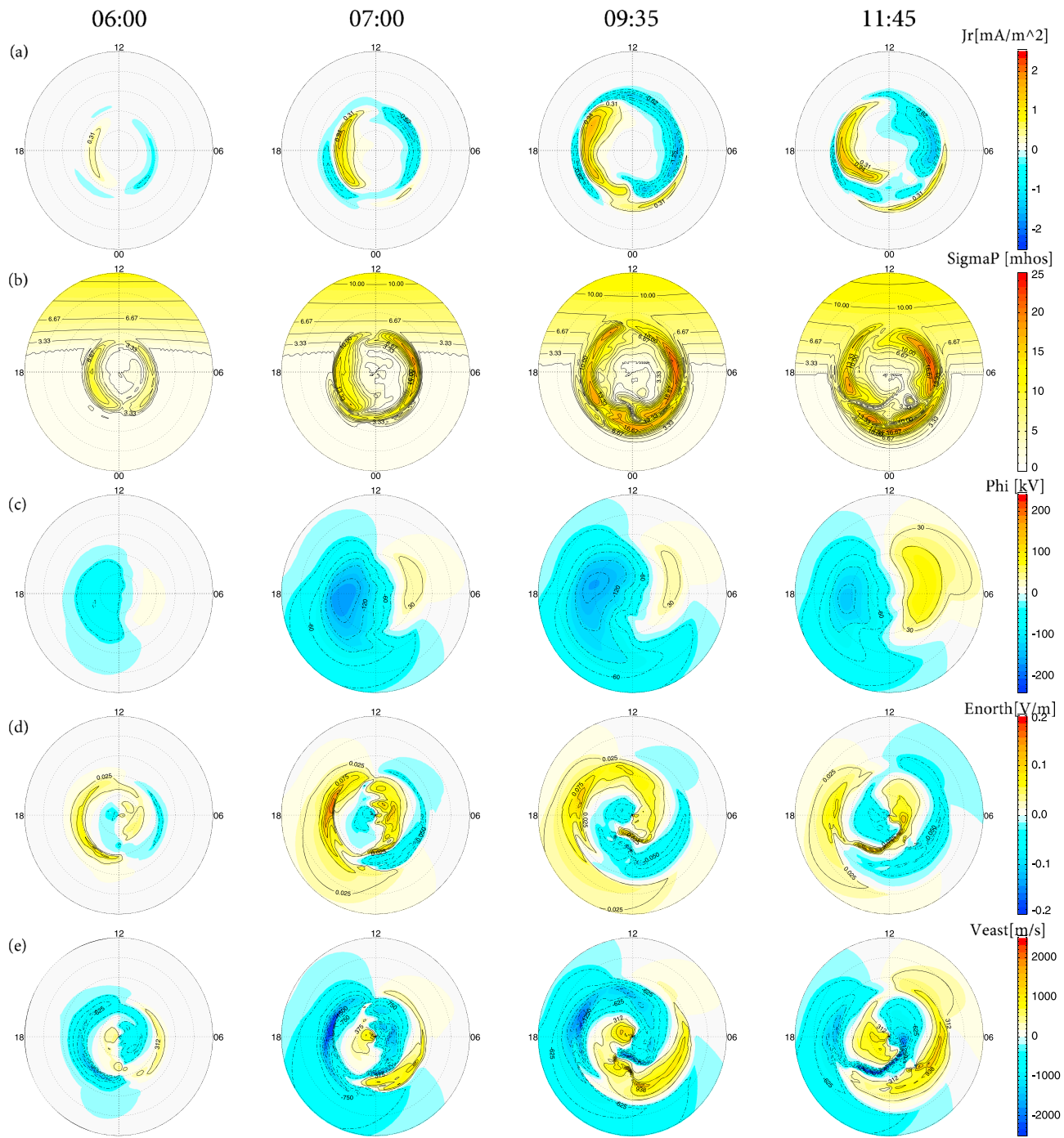


**Figure 4.** Ionospheric simulation results at selected time: (a) field-aligned currents (upward in yellow and downward in blue), (b) Pedersen conductance, (c) electric potential, (d) northward electric field in yellow and southward electric field in blue, and (e) eastward plasma convection in yellow and westward in blue. The selected time include 06:00 UT during quiet time, 07:00 UT during the storm sudden commencement, and 09:35 and 11:45 UT during the storm main phase.

Figure 5 shows the ionospheric electrodynamics at 19 MLT during the whole storm period, for magnetic latitudes above 50°. After SSC, the westward plasma convection at lower latitudes is initiated and the intensification mainly occurs after 08:00 UT, with speed larger than 1000 m/s. Such a rapidly drifting flow occurs mostly below 60° and lasts intermittently for many hours during the storm main phase. On the other hand, the high-latitude auroral westward convection that is separated from the subauroral westward streams occurs mostly above 60°. The enhanced flow in the subauroral region is found to be well collocated with

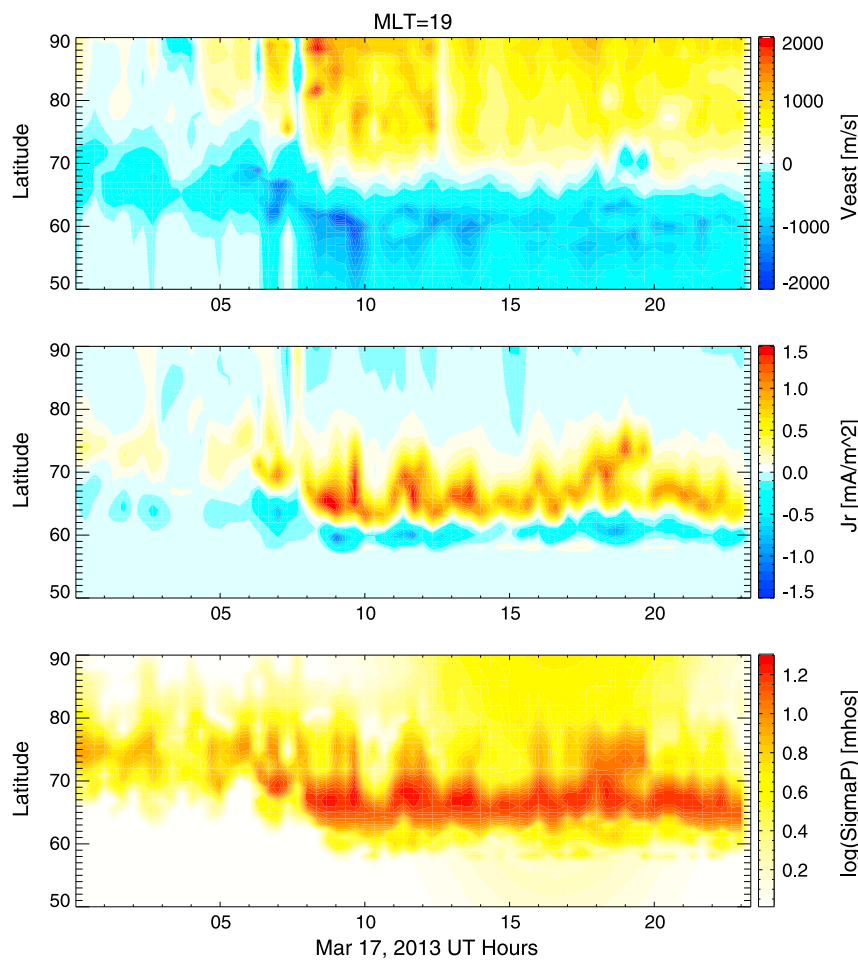


**Figure 5.** Model results at MLT of 19 in the ionosphere, as a function of magnetic latitude above 50° and UT time. (top) East-west plasma convection, (middle) up-down field-aligned current, and (bottom) Pedersen conductance.

the lower latitude part of the downward Region 2 FACs in the subauroral region where the Pedersen conductivity is lower than the auroral conductivity (see Figures 5 (middle) and 5 (bottom)). This strongly indicates that the model captures the basic physics of the SAPS [Southwood and Wolf, 1978].

It is expected that the enhanced electric field in the subauroral region can result in enhanced frictional heating and the subsequent enhanced electron temperature that lead to a larger recombination rate in the ionosphere. This could further reduce the ionospheric conductivity and therefore increase the strength of the SAPS, as suggested by Anderson *et al.* [1991]. Such feedback effects, however, are not included in the current modeling framework. The consequence is that the strength of the SAPS might be underestimated in this simulation. Future study could consider including an ionosphere-thermosphere model to account for the above feedback effect.

### 3.2. Inner Magnetospheric Dynamics

As the Region 2 FACs bridges the midlatitude ionosphere to the inner magnetosphere, the dynamics in the inner magnetosphere during the storm can be an important factor in influencing the subauroral electrodynamics. This section describes the development of the partial ring current, magnetospheric electric potential, and the penetration electric field inside  $L$  of 4, to demonstrate the magnetospheric signatures and their evolution associated with the SAPS.

Figure 6 shows ring current energy density, electric field in the radial direction, and the equipotential contour lines in the magnetic equatorial plane at the same selected times as in Figure 4. When the solar wind driving force is enhanced after SSC, tail plasma sheet particles are transported inward in association with the enhanced convection electric field. In the inner magnetosphere, the magnetic and gradient curvature

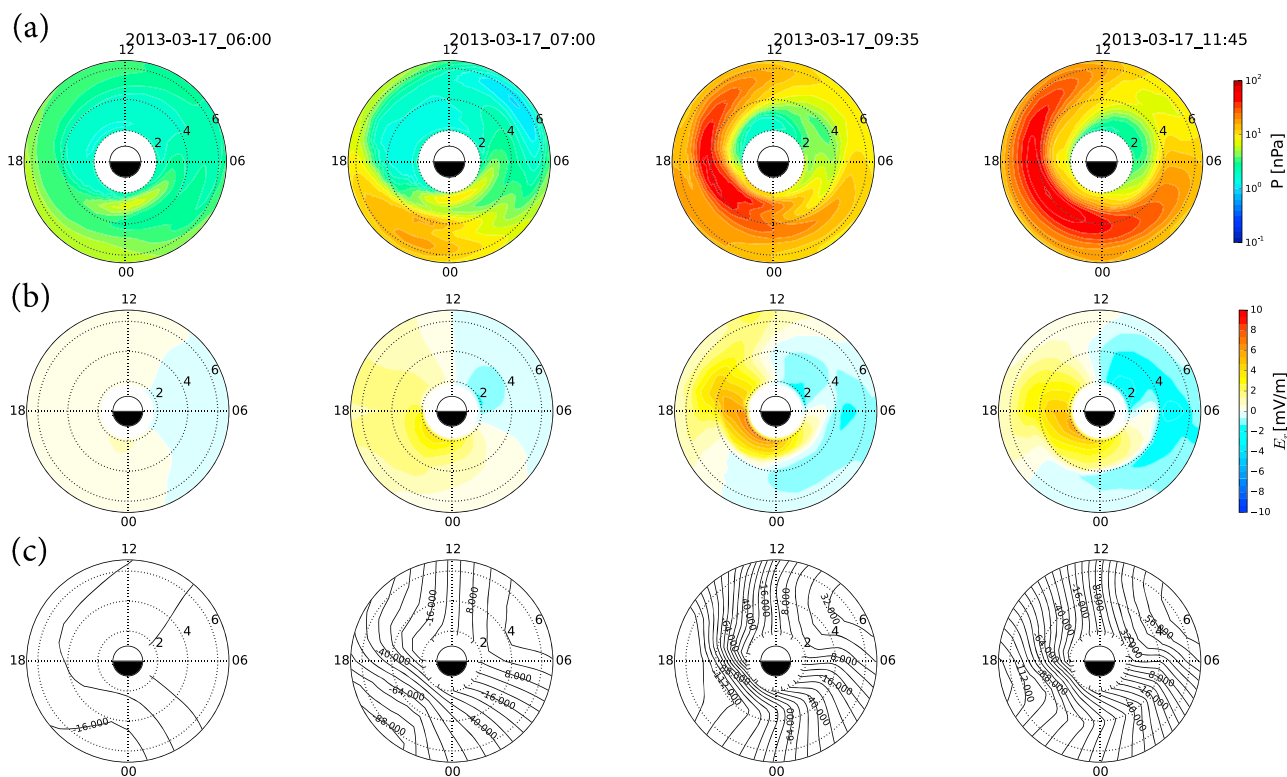


**Figure 6.** Model results in the magnetic equator inside  $L$  of 6.5 at selected time: (a) ring current energy density, (b) electric field in the radial direction (red is positive and blue is negative), and (c) the equipotential contour lines. The selected times are the same as in Figure 4.

force moves ions westward and electrons eastward. As the ions are transported deep into the inner magnetosphere while circling toward the noon meridian (see at 09:35 UT), the partial ring current is formed. The Region 2 FACs, generated by the misalignment between the ring current pressure gradient and the gradient in the magnetic flux volume, connect the partial ring current with the ionosphere and rotate westward. This rotation is already demonstrated in the ionospheric electrodynamics in Figure 4. As the ring current particles move closer to the Earth, pushing the ion plasma sheet boundary inward, the Region 2 associated electric field will move earthward as well. As discussed above, the poleward electric field in the subauroral region (Figure 4d) is significantly increased at latitudes below  $60^\circ$ ; when mapped to the inner magnetosphere, this corresponds to an increase in the radial electric field inside  $L$  of 4, as is shown in Figure 6b. The large radial electric field is confined mostly between dusk-to-midnight sector, slightly extending into postmidnight.

The global electric potential in Figure 6c shows that during disturbed time the nightside convection electric field is nearly in the dawn-to-dusk direction outside  $L$  of 4; while moving closer to the Earth, the contour lines skew westward and move closer to each other inside  $L$  of 4 especially in the dusk sector, resulting in a large radially directed electric field in the inner magnetosphere. This is consistent with observations of Rowland and Wygant [1998] who showed that duskward electric field between  $L$  of 3.0 and 5.5 in the evening local times can be considerably enhanced when  $K_p$  is high.

#### 4. Comparisons With Observations

To examine the model fidelity in reproducing the ionospheric electrodynamics in terms of FACs, subauroral plasma drift, and large-scale electric field in the inner magnetosphere associated with the SAPS, comparisons between simulation results and observations from Active Magnetosphere and Planetary Electrodynamics Response Experiment (AMPERE), Defense Meteorological Satellite Program (DMSP), and Van Allen Probes are carried out.

AMPERE provides global maps of FACs over the polar ionosphere, derived from measurements of magnetic field perturbations at Iridium altitude ( $\sim 780$  km) after applying a spherical harmonic fit. Figures 7a and 7b show the magnetic field perturbation induced by FACs and global FACs patterns at 07:00 UT and 09:35 UT in

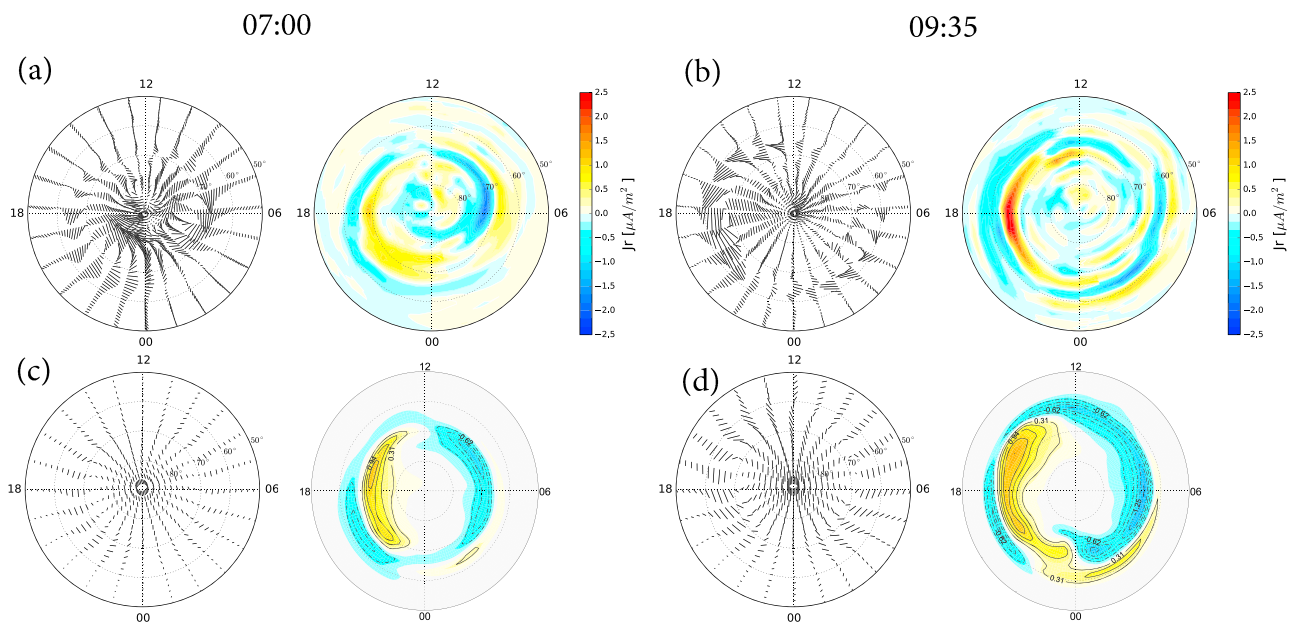


**Figure 7.** (a, b) Horizontal magnetic field perturbations observed by Iridium satellites after spherical harmonic fit and AMPERE-derived field-aligned currents (FACs) patterns at 07:00 and 09:35 UT during the 17 March 2013 storm event. (c, d) Simulated horizontal magnetic field perturbations at the Iridium altitude and the associated field-aligned currents. Yellow indicates upward current, and blue indicates downward current. The circles are plotted above 50°.

the Northern Hemisphere. The two-pair FACs pattern generally agrees with the simulation results shown in Figures 7c and 7d in terms of the magnitude and location. Region 2 FACs are slightly above 60° and Region 1 FACs are centered around 70°. At the highly disturbed time (09:35 UT), while the observation depicts fine structures, some general features are still identified: both Regions 1 and 2 FACs are enhanced; the currents shift to lower latitudes (i.e., the auroral oval expands); the Region 2 currents rotate westward. All these phenomena are reproduced by the simulation. The vector plots illustrate the horizontal magnetic field perturbations induced by field-aligned currents at the Iridium altitude. Although the simulated perturbations (Figures 7c and 7d) show less structures, their comparisons with the measurements (Figures 7a and 7b) demonstrate the agreement on the location of currents and comparable magnitude (vector length) of the perturbations.

DMSP satellites measure ion horizontal drift velocity component perpendicular to the satellite trajectory at altitude of 830 km as well as particle precipitating fluxes. F17 and F18 spacecraft were orbiting across the dusk-dawn meridian during the storm main phase of the 17 March 2013 storm. Figure 8 shows comparisons between DMSP measurements and model prediction of the drift velocity along two consecutive orbits of both satellites over the Northern Hemisphere, from the duskside toward the dawnside across the polar cap. The velocity is plotted in the Y direction in the satellite coordinates, perpendicular to the satellite trajectory. Each orbit shows that the satellite flies through the two-cell auroral convection: sunward convection in the dusk sector, antisunward convection over the polar cap, and sunward convection in the dawn sector. The vertical dashed lines mark the equatorward boundary of the auroral zone, which is the edge where the electron fluxes sharply increase along the rising satellite trajectory, as identified from the electron precipitating fluxes. The double-peak westward drift profiles in the DMSP observations on the dusk side are well separated across this boundary in most cases (except for Figure 8c), indicating that the lower latitude westward flow is in the subauroral region and confirms its SAPS nature. From the line plots, it is found that the model is capable of reasonably capturing the location of the two-cell pattern, the position and the latitudinal width of the rapid sunward drift in the dusk sector. However, the model underestimates the magnitude of the drift and misses the bifurcate feature of the flow along these trajectories, although the simulation indeed demonstrates a double-channel convection pattern in the dusk sector but at later local times (see Figures 4e and 5). This indicates that the model is incapable of accurately reproducing the exact location of the subauroral streams. This might be attributed to the lack of thermosphere-ionosphere coupling in the model which could not only amplify the intensity of the SAPS but also push the SAPS toward the dayside. Nevertheless, the model captures the mechanism of the SAPS as illustrated in the circular plots

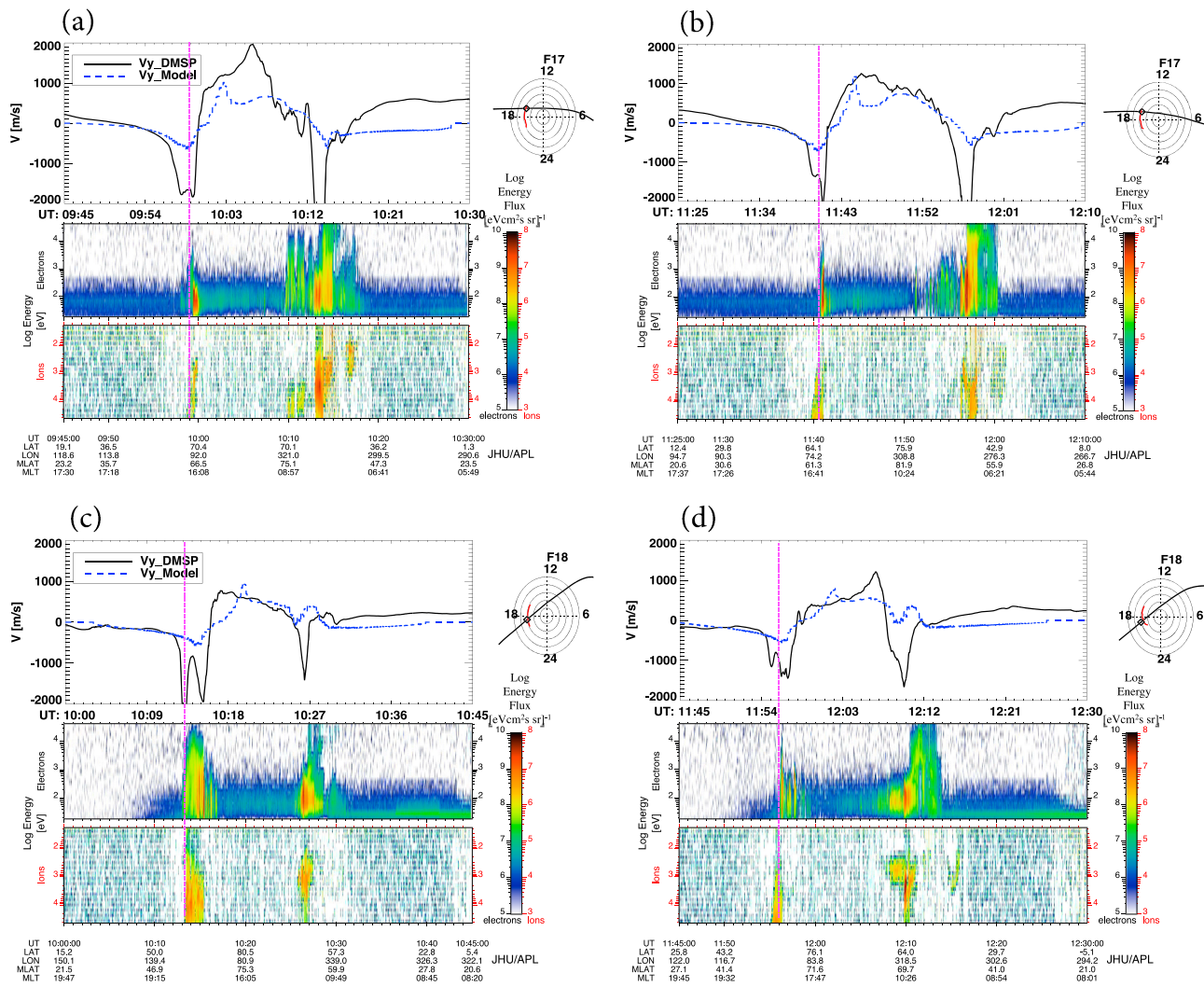


**Figure 8.** (a–d) The ion drift velocity and particle precipitation along DMSP trajectories during four periods when the satellites fly across the Northern Hemisphere. Line plots illustrate comparisons of ion drift velocity between DMSP measurement (solid) and simulation results (dashed). The Y direction of the velocity is perpendicular to the spacecraft trajectory. Negative velocity represents sunward drift. The color plots demonstrate the DMSP measured auroral electron and ion precipitating fluxes. The vertical dash lines mark the equatorward boundary of the auroral zone where the precipitating electron fluxes sharply increase along the rising trajectory. The orbits are shown on the right, flying from the dusk toward the dawn over the northern polar cap. Each circles are separated by 10°. The red curve in each circles represents the equatorward edge of the simulated electron precipitation/upward Region 1 FACs, and the diamond symbol marks the location of the simulated peak flow on the trajectory.

for each trajectories, because the simulated flow peak along the trajectory (marked by the diamond symbol) appears near the equatorward edge (shown by the red curve for MLT from 16 to 20) of the simulated electron precipitation/upward Region 1 FACs, similarly to that in the observations.

The Electric Field and Waves Instruments (EFW) [Wygant *et al.*, 2013] on board Van Allen Probes provides measurements of the large-scale electric field near the magnetic equator in the inner magnetosphere. Around 10:00 UT, the Van Allen Probes-B flew across the subauroral region near the magnetic equator from dayside to the nightside and observed a localized electric field up to 12 mV/m in the SM Y component (black line in Figure 9a). Around the same time, the satellite successively passed the ion and electron plasmasheet inner boundaries as the on board Helium, Oxygen, Proton, and Electron (HOPE) instrument [Spence *et al.*, 2013] first observed sharp increases in the 5 keV proton flux and then in the 1 keV electron flux (these energies are often used to determine the plasmasheet boundary [Thomsen *et al.*, 2002; Cao *et al.*, 2011]). The narrow separation between the ion plasmasheet inner boundary and electron plasmasheet inner boundary implies a large radially outward electric field, that is, the SAPS electric field. The model similarly shows the separation of the inner edges of the ion plasmasheet and electron plasmasheet and also predicts

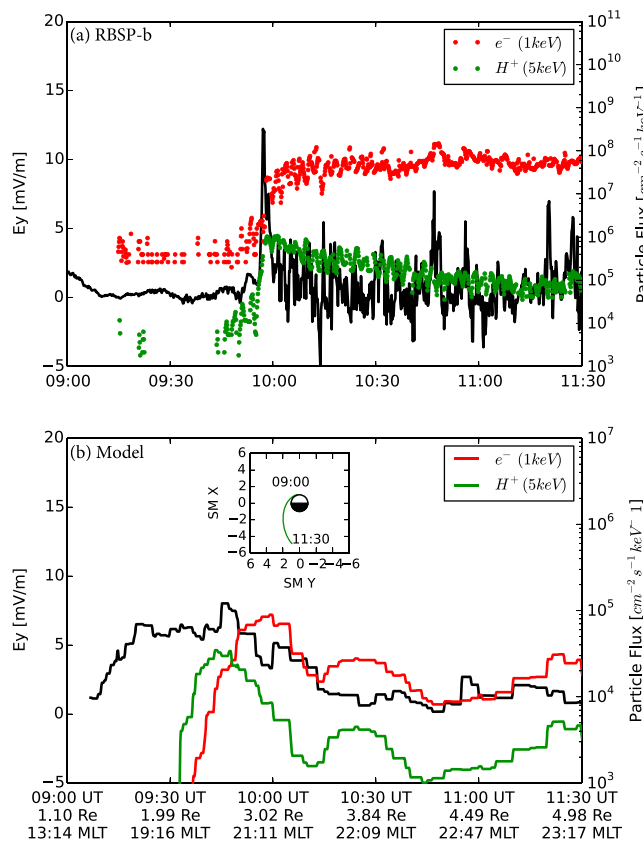


**Figure 9.** (a) The observed electron (red) and proton (green) fluxes at energy of 1 keV and 5 keV, respectively, by HOPE instrument and the  $Y$  component (duskward) of electric field (black) by the EFW instrument on board the Van Allen Probe-B spacecraft flying outbound. The rapid increase in the proton flux appears earlier than that in the electron flux, indicating that the proton plasmasheet inner boundary is more earthward than the electron plasmasheet inner boundary. The large localized electric field is induced in between the two inner boundaries. (b) Simulated electron (red) and proton (green) flux and duskward electric field (black) along the Van Allen Probe-B trajectory. The electric field is enhanced up to 8 mV/m earthward of the inner edge of the electron plasmasheet and extends further inward. The satellite moves from the dayside perigee to the nightside, passing the dusk-to-midnight sector from  $L$  of 2.0 near 19 MLT to  $L$  of 3.5 near 22 MLT.

Region 2 FACs flowing into subauroral regions where conductance is lower than that in the auroral latitudes. The electric potential cell in the evening sector extends to lower latitudes and early morning regions from its high-latitude auroral convection cell, resulting in double westward flow channels in the dusk local times. The westward flow at subauroral latitudes is well collocated with the lower latitude downward Region 2 FACs and the region with low ionospheric conductivity, strongly suggesting that the basic physics of the SAPS is represented in the model. The inner magnetosphere experiences a large electric field in the radial direction inside  $L$  of 4 in the dusk-to-midnight region, conjugate to the poleward electric field in the subauroral ionosphere that drives the SAPS.

Comparison of the simulated FACs pattern with observations from AMPERE indicates a consistent picture in the evolution of the current systems. Horizontal magnetic field perturbations induced from the FACs in the model also show comparable magnitude and location of the currents to the measured perturbations. The model also captures the mechanism of the SAPS because the simulated westward streams peak near the equatorward edge of the electron precipitation/upward Region 1 FACs, similar to the measurements from DMSP. Furthermore, similar to what was observed by the Van Allen Probes, the model shows a

increase in the duskward electric field upto 8 mV/m in between the two boundaries (Figure 9b). This strongly suggests that the model captures the mechanism of the SAPS electric field. However, it is found that the enhanced electric field appears slightly earthward of the observed location and extends toward the Earth for  $1 R_E$ . It means the modeled electric field penetrates deeper toward the Earth, suggesting that the shielding by Region 2 FACs in the model is insufficient. One reason for this discrepancy could be that the shielding of the electric field is not directly provided by the RAM-SCB Region 2 FACs, but rather by that calculated from the MHD code which is weaker and diffuser, even when the MHD code is coupled with a kinetic code [De Zeeuw et al., 2004; Zaharia et al., 2010]. A direct coupling of the stronger Region 2 FACs feedback to the ionosphere will probably lead to a stronger shielding on the inner magnetosphere and therefore will modify the ionospheric electric potential patterns as well as the penetration electric fields.

## 5. Discussion and Summary

This study carried out a simulation of the coupled magnetosphere-ionosphere system during the 17 March 2013 storm event to investigate the temporal/spatial evolution of the SAPS and the conjugate dynamics in the magnetosphere-ionosphere system. The storm time ring current development results in enhanced, expanded

separation of ion and electron plasmasheet inner boundaries and an increase in the SAPS electric field in between the two boundaries, suggesting that the mechanism of SAPS is well captured by the model. However, limitations are found from the model results. The modeled magnitude of the flow is underestimated and the bifurcate flow feature is not as clear along the DMSP trajectories although the model does show double flow channels but at other local times. The modeled SAPS electric field in the inner magnetosphere displays a much larger spatial extent inside  $L$  of 3. This deep penetration of electric field suggests an insufficient Region 2 FACs shielding in the model. The much broader latitudinal width in the model may also imply that the model resolution used in this study ( $0.25 R_E$  in the inner magnetosphere and  $1^\circ$  latitude in the ionosphere) could be another obstacle to resolving such a localized electrodynamics of SAPS.

This study presented a state-of-the-art coupling approach of the magnetosphere-ionosphere system in reproducing the inner magnetospheric and the subauroral ionospheric dynamics. Comparisons of the simulation results with observations helped us identify the deficiencies in the current modeling capability and propose possible solutions for future improvement. While the dynamic interchange between the ionosphere and the magnetosphere appears to be represented in the model, the self-consistent relation in the ionospheric conductance with particle precipitation is presently missing, although the employed empirical formula in specifying the conductance is currently state of the art. Also, the underestimated intensity of SAPS in the ionosphere might be modified after taking into account the thermosphere-ionosphere chemical processes. Therefore, future studies will be directed to implement a self-consistent treatment of ionospheric conductivity from particle precipitation, to couple the ionospheric electrodynamics with a thermosphere-ionosphere module, and to connect the ionosphere with the inner magnetosphere by the Region 2 FACs calculated directly from the inner magnetosphere model for a better electric field shielding. These would potentially improve the model performance in capturing the realistic subauroral electrodynamics.

#### Acknowledgments

This work was supported by NASA grant AGRNNH14AX901 and JHU/APL contracts 967399 and 921647 under NASA's primer contract NAS5-01072. S. Zou is supported by NSF AGS1111476, AGS1203232, and AGS1342968. The analysis at LANL was also supported by EMFISI subaward NNG13PJ05I and by the Laboratory Directed Research and Development (LDRD) program. We thank the OMNIWeb from NASA Goddard Space Flight Center for providing the solar wind observation data and the Kyoto, Japan, World Data Center System for providing the SYM-H index. We thank the AMPERE team and AMPERE Science Center for providing the Iridium-derived data products. The DMSP particle detectors were designed by Dave Hardy of AFRL, and data obtained from JHU/APL. All Van Allen Probes data used are publicly available at NASA CDAWeb ([http://cdaweb.gsfc.nasa.gov/istp\\_public/](http://cdaweb.gsfc.nasa.gov/istp_public/)).

Larry Kepko thanks the reviewers for their assistance in evaluating this paper.

#### References

- Anderson, P. C., R. A. Heelis, and W. B. Hanson (1991), The ionospheric signatures of rapid subauroral ion drifts, *J. Geophys. Res.*, 96(A4), 5785–5792, doi:10.1029/90JA02651.
- Anderson, P. C., D. L. Carpenter, K. Tsuruda, T. Mukai, and F. J. Rich (2001), Multisatellite observations of rapid subauroral ion drifts (said), *J. Geophys. Res.*, 106(A12), 29,585–29,599, doi:10.1029/2001JA000128.
- Baumjohann, W., G. Paschmann, and C. A. Cattell (1989), Average plasma properties in the central plasma sheet, *J. Geophys. Res.*, 94(A6), 6597–6606, doi:10.1029/JA094iA06p06597.
- Cao, J. B., W. Z. Ding, H. Reme, I. Dandouras, M. Dunlop, Z. X. Liu, and J. Y. Yang (2011), The statistical studies of the inner boundary of plasma sheet, *Ann. Geophys.*, 29(2), 289–298, doi:10.5194/angeo-29-289-2011.
- Clausen, L. B. N., et al. (2012), Large-scale observations of a subauroral polarization stream by midlatitude SUPERDARN radars: Instantaneous longitudinal velocity variations, *J. Geophys. Res.*, 117, A05306, doi:10.1029/2011JA017232.
- De Zeeuw, D. L., S. Sazykin, R. A. Wolf, T. I. Gombosi, A. J. Ridley, and G. Tóth (2004), Coupling of a global MHD code and an inner magnetospheric model: Initial results, *J. Geophys. Res.*, 109, A12219, doi:10.1029/2003JA010366.
- Ebihara, Y., N. Nishitani, T. Kikuchi, T. Ogawa, K. Hosokawa, M.-C. Fok, and M. F. Thomsen (2009), Dynamical property of storm time subauroral rapid flows as a manifestation of complex structures of the plasma pressure in the inner magnetosphere, *J. Geophys. Res.*, 114, A01306, doi:10.1029/2008JA013614.
- Fok, M.-C., R. A. Wolf, R. W. Spiro, and T. E. Moore (2001), Comprehensive computational model of Earth's ring current, *J. Geophys. Res.*, 106, 8417–8424, doi:10.1029/2000JA000235.
- Foster, J. C., and W. J. Burke (2002), SAPS: A new categorization for sub-auroral electric fields, *Eos Trans. AGU*, 83(36), 393–394, doi:10.1029/2002EO000289.
- Foster, J. C., and W. Rideout (2007), Storm enhanced density: Magnetic conjugacy effects, *Ann. Geophys.*, 25(8), 1791–1799, doi:10.5194/angeo-25-1791-2007.
- Foster, J. C., and H. B. Vo (2002), Average characteristics and activity dependence of the subauroral polarization stream, *J. Geophys. Res.*, 107(A12), 1475, doi:10.1029/2002JA009409.
- Foster, J. C., P. J. Erickson, A. J. Coster, S. Thaller, J. Tao, J. R. Wygant, and J. W. Bonnell (2014), Storm time observations of plasmasphere erosion flux in the magnetosphere and ionosphere, *Geophys. Res. Lett.*, 41, 762–768, doi:10.1002/2013GL059124.
- Garner, T. W., R. A. Wolf, R. W. Spiro, W. J. Burke, B. G. Fejer, S. Sazykin, J. L. Roeder, and M. R. Hairston (2004), Magnetospheric electric fields and plasma sheet injection to low  $L$ -shells during the 4–5 June 1991 magnetic storm: Comparison between the rice convection model and observations, *J. Geophys. Res.*, 109, A02214, doi:10.1029/2003JA010208.
- Gkioulidou, M., C.-P. Wang, and L. R. Lyons (2011), Effect of self-consistent magnetic field on plasma sheet penetration to the inner magnetosphere: Rice convection model simulations combined with modified Dungey force-balanced magnetic field solver, *J. Geophys. Res.*, 116, A12213, doi:10.1029/2011JA016810.
- Goldstein, J., J. L. Burch, and B. R. Sandel (2005), Magnetospheric model of subauroral polarization stream, *J. Geophys. Res.*, 110, A09222, doi:10.1029/2005JA011135.
- Jordanova, V. K., Y. S. Miyoshi, S. Zaharia, M. F. Thomsen, G. D. Reeves, D. S. Evans, C. G. Mouikis, and J. F. Fennell (2006), Kinetic simulations of ring current evolution during the Geospace Environment Modeling challenge events, *J. Geophys. Res.*, 111, A11S10, doi:10.1029/2006JA011644.
- Jordanova, V. K., S. Zaharia, and D. T. Welling (2010), Comparative study of ring current development using empirical, dipolar, and self-consistent magnetic field simulations, *J. Geophys. Res.*, 115, A00J11, doi:10.1029/2010JA015671.

- Jordanova, V. K., D. T. Welling, S. G. Zaharia, L. Chen, and R. M. Thorne (2012), Modeling ring current ion and electron dynamics and plasma instabilities during a high-speed stream driven storm, *J. Geophys. Res.*, 117, A00L08, doi:10.1029/2011JA017433.
- Karlsson, T., G. T. Marklund, L. G. Blomberg, and A. Mälki (1998), Subauroral electric fields observed by the Freja satellite: A statistical study, *J. Geophys. Res.*, 103(A3), 4327–4341, doi:10.1029/97JA00333.
- Lemon, C., F. Toffoletto, M. Hesse, and J. Birn (2003), Computing magnetospheric force equilibria, *J. Geophys. Res.*, 108(A6), 1237, doi:10.1029/2002JA009702.
- Oksavik, K., R. A. Greenwald, J. M. Ruohoniemi, M. R. Hairston, L. J. Paxton, J. B. H. Baker, J. W. Gjerloev, and R. J. Barnes (2006), First observations of the temporal/spatial variation of the sub-auroral polarization stream from the SUPERDARN wallops hf radar, *Geophys. Res. Lett.*, 33, L12104, doi:10.1029/2006GL026256.
- Powell, K. G., P. L. Roe, T. J. Linde, T. I. Gombosi, and D. L. D. Zeeuw (1999), A solution-adaptive upwind scheme for ideal magnetohydrodynamics, *J. Comput. Phys.*, 154, 284–309.
- Richmond, A. D., and Y. Kamide (1988), Mapping electrodynamic features of the high-latitude ionosphere from localized observations: Technique, *J. Geophys. Res.*, 93(A6), 5741–5759, doi:10.1029/JA093iA06p05741.
- Ridley, A. J., T. I. Gombosi, and D. L. D. Zeeuw (2004), Ionospheric control of the magnetospheric configuration: Conductance, *Ann. Geophys.*, 22, 567–584.
- Rowland, D. E., and J. R. Wygant (1998), Dependence of the large-scale, inner magnetospheric electric field on geomagnetic activity, *J. Geophys. Res.*, 103(A7), 14,959–14,964, doi:10.1029/97JA03524.
- Ruohoniemi, J. M., and K. B. Baker (1998), Large-scale imaging of high-latitude convection with super dual auroral radar network hf radar observations, *J. Geophys. Res.*, 103(A9), 20,797–20,811, doi:10.1029/98JA01288.
- Southwood, D. J., and R. A. Wolf (1978), An assessment of the role of precipitation in magnetospheric convection, *J. Geophys. Res.*, 83(A11), 5227–5232, doi:10.1029/JA083iA11p05227.
- Spence, H., et al. (2013), Science goals and overview of the Radiation Belt Storm Probes (RBSP) Energetic Particle, Composition, and Thermal Plasma (ECT) suite on NASA's Van Allen Probes mission, *Space Sci. Rev.*, 179, 311–336, doi:10.1007/s11214-013-0007-5.
- Spiro, R. W., R. A. Heelis, and W. B. Hanson (1978), Ion convection and the formation of the mid-latitude F region ionization trough, *J. Geophys. Res.*, 83(A9), 4255–4264, doi:10.1029/JA083iA09p04255.
- Thomsen, M. F., H. Korth, and R. C. Elphic (2002), Upper cutoff energy of the electron plasma sheet as a measure of magnetospheric convection strength, *J. Geophys. Res.*, 107(A10), 1331, doi:10.1029/2001JA000148.
- Toffoletto, F., S. Sazykin, R. Spiro, and R. Wolf (2003), Inner magnetospheric modeling with the rice convection model, *Space Sci. Rev.*, 107, 175–196, doi:10.1023/A:1025532008047.
- Tsyganenko, N. A. (1989), A magnetospheric magnetic field model with a warped tail current sheet, *Planet. Space Sci.*, 37, 5–20, doi:10.1016/0032-0633(89)90066-4.
- Wang, H., A. J. Ridley, H. Lühr, M. W. Liemohn, and S. Y. Ma (2008), Statistical study of the subauroral polarization stream: Its dependence on the cross-polar cap potential and subauroral conductance, *J. Geophys. Res.*, 113, A12311, doi:10.1029/2008JA013529.
- Wang, H., S.-Y. Ma, and A. J. Ridley (2009), Comparative study of subauroral polarization streams with dmsp observation and ram simulation, *Chinese J. Geophys.*, 52(3), 531–540, doi:10.1002/cjg2.1374.
- Wygant, J., et al. (2013), The electric field and waves instruments on the radiation belt storm probes mission, *Space Sci. Rev.*, 179(1–4), 183–220, doi:10.1007/s11214-013-0013-7.
- Yeh, H.-C., J. C. Foster, F. J. Rich, and W. Swider (1991), Storm time electric field penetration observed at mid-latitude, *J. Geophys. Res.*, 96(A4), 5707–5721, doi:10.1029/90JA02751.
- Young, D. T., H. Balsiger, and J. Geiss (1982), Correlations of magnetospheric ion composition with geomagnetic and solar activity, *J. Geophys. Res.*, 87(A11), 9077–9096, doi:10.1029/JA087iA11p09077.
- Zaharia, S., V. K. Jordanova, M. F. Thomsen, and G. D. Reeves (2006), Self-consistent modeling of magnetic fields and plasmas in the inner magnetosphere: Application to a geomagnetic storm, *J. Geophys. Res.*, 111, A11S14, doi:10.1029/2006JA011619.
- Zaharia, S., V. K. Jordanova, D. Welling, and G. Tóth (2010), Self-consistent inner magnetosphere simulation driven by a global MHD model, *J. Geophys. Res.*, 115, A12228, doi:10.1029/2010JA015915.
- Zheng, Y., P. C. Brandt, A. T. Y. Lui, and M.-C. Fok (2008), On ionospheric trough conductance and subauroral polarization streams: Simulation results, *J. Geophys. Res.*, 113, A04209, doi:10.1029/2007JA012532.
- Zou, S., A. J. Ridley, M. B. Moldwin, M. J. Nicolls, A. J. Coster, E. G. Thomas, and J. M. Ruohoniemi (2013), Multi-instrument observations of SED during 24–25 October 2011 storm: Implications for SED formation processes, *J. Geophys. Res. Space Physics*, 118, 7798–7809, doi:10.1002/2013JA018860.